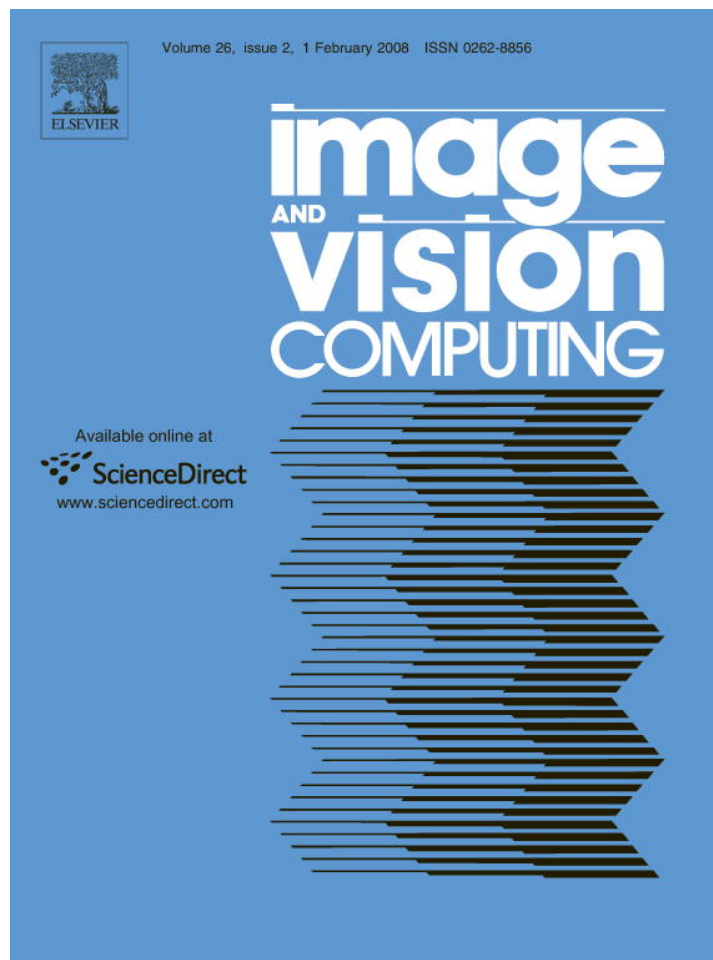


Provided for non-commercial research and education use.
Not for reproduction, distribution or commercial use.



This article was published in an Elsevier journal. The attached copy is furnished to the author for non-commercial research and education use, including for instruction at the author's institution, sharing with colleagues and providing to institution administration.

Other uses, including reproduction and distribution, or selling or licensing copies, or posting to personal, institutional or third party websites are prohibited.

In most cases authors are permitted to post their version of the article (e.g. in Word or Tex form) to their personal website or institutional repository. Authors requiring further information regarding Elsevier's archiving and manuscript policies are encouraged to visit:

<http://www.elsevier.com/copyright>



Parallelized segmentation of a serially sectioned whole human brain

Oliver Schmitt ^{a,*}, Sven Bethke ^{b,1}, Peter Sobe ^b, Steffen Prehn ^b, Erik Maehle ^b

^a *Institute of Anatomy, Gertrudenstraße 9, 18055 Rostock, Germany*

^b *Institute of Computer Engineering, Ratzeburger Allee 160, 23538 Lübeck, Germany*

Received 12 February 2006; received in revised form 7 April 2007; accepted 1 June 2007

Abstract

Building a digital three dimensional representation of a human brain is a challenging task. Such a model provides insights into the microstructure of cortical layering and columns. The presented work is based on a complete dissected and preserved human brain that has been serially sectioned at a coronal resolution that is suitable for single cell detection. More than 6000 sections have been generated and exist as digital images. To obtain a valuable three dimensional representation, morphology preserving affine linear and nonlinear registration schemes are necessary steps. To rebuild a serially sectioned brain, reference images derived from a non deformed object, e.g., MRI or block face images, are necessary for a faithful affine linear and nonlinear registration. In the case of block face images the brain regions must be separated from highly variable background regions to obtain a suitable stack of segmentation images. Among the image segmentation algorithms we found fuzzy c-means techniques as a promising starting point for a sophisticated segmentation framework of either gray level or color images within 2- and 3-dimensions.

With respect to algorithmic complexity and computation cost, two fuzzy c-means algorithms were implemented. A proper image pre-processing strategy turned out to be necessary for accurate and robust segmentation results. Primarily, the algorithms work in a parametric resp. supervised mode. Additionally, an automatic mode helps to explore the parameter space within a reasonable range and to compare the segmentation result with an optimal one, provided by an expert. By minimizing the differences we can set up parameters that are used for series of adjacent images. So, it is possible to obtain optimal segmentations independent of illumination disturbances, artifacts and defocusing.

We present a complete high resolution and accurate segmentation of the first complete human brain that was sectioned, photographed and digitized at histologic resolution. Based on these images, a succeeding 3D representation is presented. Finally, a segmented and spatially correct straightened data set is available now for coregistration tasks together with the high resolution histologic data set.

© 2007 Elsevier B.V. All rights reserved.

Keywords: Segmentation; Adaptive fuzzy c-means; Human brain; Paraffin sections; Histologic sections; Block-face; Episcopic images

1. Introduction

Information of structural modalities of a biological object at high spatial resolution, i.e., $x_r, y_r, z_r \leq 100 \mu\text{m}$, have a strong impact for providing frameworks for mapping and coregistration of other modalities derived from RNA- and protein-expressions [21]. To obtain data from

mammal brains at this resolution, it is necessary to dissect them by histologic techniques. This yields to a partial loss of spatial information from the macro-, through the meso- down to the microscale. The preparation of a serially sectioned brain is followed by histologic procedures that are in particular determined by the structures, functional or the molecular modalities which are to visualize. The results are digitized by videomicroscopic mosaicing or high resolution transparent flat bed scanning. The stack of images must be preprocessed before alignment of the images is performed. The most important procedure is a segmentation of the foreground of the images. Further steps of preprocessing are discussed by Modersitzki [23]. The rigid, linear

* Corresponding author.

E-mail addresses: schmitt@med.uni-rostock.de (O. Schmitt), syb28975@gsk.com (S. Bethke), sobe@iti.uni-luebeck.de (P. Sobe), prehn@iti.uni-luebeck.de (S. Prehn), maehle@iti.uni-luebeck.de (E. Maehle).

¹ Present address: Glaxo Wellcome GmbH & Co., Industriestraße 32-36, D-23843 Bad Oldesloe, Germany.

affine or nonlinear alignment [10,23] of such a preprocessed image stack may introduce deformations because the information of the global shape of the object is lost or loss of the information between furthest foreground objects apart is largest. Large image stacks consisting of relative thin sections will yield to larger registration based deformations than small image stacks of the same object with thick sections. To solve this problem reference sections at a lower resolution that have a correct spatial relation to each other can be used to register deformed high resolution images, i.e., template images. Ideally, a direct template to reference alignment can be performed if each reference section has a template section counterpart. Thus, deformations introduced by the registration technique can be avoided [45,26,25,11,5].

In this study, a stack of reference images was preprocessed to obtain images for the step of coregistration with histological images. The reference images were derived from the surface of the serially sectioned paraffin block containing the embedded brain. However, the so-called block-face or episcopic images contain several structures which have to be assigned to the background. According to the relative transparency of the embedding material, illumination disturbances and sectioning problems over 6200 whole brain sections the segmentation of the foreground becomes a challenging task. Conventional segmentation algorithms [15,17,35,50,24,37,43,27,52,53] mainly based on threshold and local adaptive techniques seem to be improperly. A statistical pixel classifier based on random fields [51,44], adaptive weight smoothing [33], adaptive segmentation via expectation–maximization [49] and fuzzy c-means segmentation [28–31] are more promising. A review of statistical methods for brain segmentation is provided by Bezdek [8] and further segmentation methods can be found in [3], however, most techniques are developed for gray scale MR image segmentation.

In this study, a reliable segmentation of the stack of color images turns out to be impossible by using standard segmentation approaches. This is due to different artifacts in the images which emerged within sectioning the embedded brain over a period of one year. In particular these artifacts are noise, variation of the illumination intensity, partly inhomogeneous illumination, small shifts of the holder of the paraffin block and variations of camera focus. A further problems that hampered conventional segmentation was the relative transparency of the paraffin wax. This phenomenon makes it difficult to classify pixels around the contour of the brain. It is comparable with partial volume averaging known from MRI-scanning where multiple tissues are present in a single pixel. In several publications [28–31] it was shown that soft segmentation methods combining clustering techniques with fuzzy set approaches give rise to superior classification results in comparison to conventional segmentation algorithms. Motivated by these promising studies soft segmentation methods were adapted to color images derived from serial block-face sections.

The key contribution of this work consists in image segmentations based on *Adaptive Fuzzy C-Means* (AFCM) and on *Fuzzy and Noise Tolerant Adaptive Segmentation* (FANTASM), provided in a fast parallel implementation for a shared memory architecture. Additionally, an optimization technique for unsupervised parameter estimation for AFCM and FANTASM was developed. This automatic segmentation framework then has been applied to a real world problem, particularly the segmentation of a complete series of 6213 block-face images of a human brain. Finally, we present a 3D-reconstruction of the segmented stack of reference images.

2. Material and methods

2.1. Material

The brain of a neurologic normal 65 year old female volunteer (Body Donor Program, Institute of Anatomy, University of Lübeck, Germany) was dissected post mortem. A whole brain immersion fixation in a buffered formaldehyde (PBS, pH 7.4, 0.9% NaCl) solution for 3 months followed by embedding in paraffin wax. Sections of 20 μm thickness were cut by a sliding microtome (Fig. 1).

2.2. Imaging

Before each sectioning a high resolution episcopic image (EPI) from the block-face of the paraffin block was produced from a scanner camera that is placed directly over

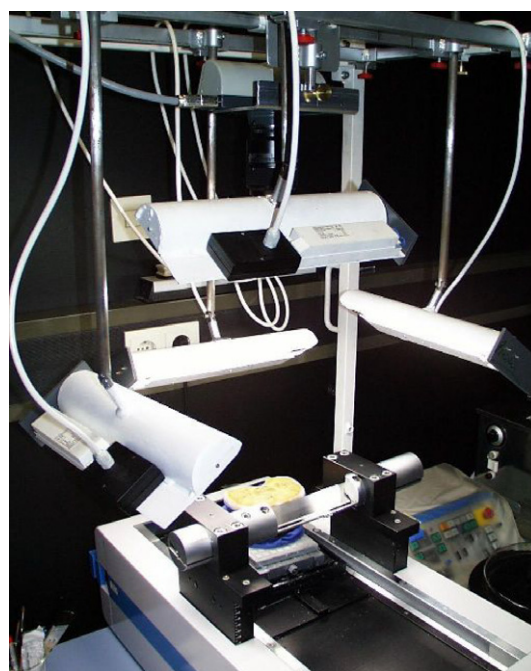


Fig. 1. Over the microtome the scanner camera is mounted surrounded from daylight fluorescent tubes. The paraffin block is just below the scanner camera in the stop position from where it is traced back to the front of the sliding microtome.

the stop position of the paraffin block (Fig. 1). The RGB-image has an external resolution of 1352×1795 pixels with a dynamic range of 8 Bits per color channel. The technical features of the illumination with daylight characteristics are described by Schmitt [39].

2.3. Preprocessing

2.3.1. Color processing

The digital images used here are represented in matrices (b) $b_{(x,y)} \in I$ whereby the intensities (I) $I = \{0, \dots, 2^k - 1\}$ have a k -Bit range. Here, three channel images $P_{(x,y)}$ are presented by three matrices b . For an image size of $m \times n$ -pixel the matrix has its origin at $b_{0,0}$ is defined as follows:

$$B = \begin{bmatrix} b_{0,0} & \cdots & b_{0,m-1} \\ \vdots & \ddots & \vdots \\ b_{n-1,0} & \cdots & b_{n-1,m-1} \end{bmatrix}$$

The RGB-image consists of the matrices B^R , B^G and B^B whereby the value of a pixel at (x, y) is given by the vector

$$P_{(x,y)} = \begin{pmatrix} b_{x,y}^R \\ b_{x,y}^G \\ b_{x,y}^B \end{pmatrix}$$

Among the color spaces RGB, CIEXYZ, CIELUV, CIE-LAB, YUV, YIQ, HSV, HSL [38] we observed in the case of the image set under work that a transformation of the color images to gray value images can be performed optimal with respect to contrast preservation using a weighted mixture of the RGB, HSL (hue lightness, saturation) and HSV (hue, saturation, value) models:

$$P_{(x,y)}^{\text{gray}} = 0.3 \cdot P_{(x,y)}^{\text{RGB-B}} + 0.5 \cdot P_{(x,y)}^{\text{HLS-L}} - 0.6 \cdot P_{(x,y)}^{\text{HSV-V}}$$

Note, that the value channel HSV-V is subtracted in this model. An original EPI image and the resulting color transformation is shown in Fig. 2. This is followed by a normalization to a 8-Bit gray level image.

The distribution of intensities was stretched according to

$$T(i) = 255 \cdot H(i) = \frac{255}{M \cdot N} \sum_{\epsilon=0}^i h(\epsilon) \quad (1)$$

whereby $h(\epsilon)$ is the histogram of the image and $H(i)$ the cumulative distribution function of the histogram. This transformation that enlightens dark image regions and increases the contrast is applied to each pixel.

$$\hat{I}(x, y) = T(I(x, y)) \quad (2)$$

2.3.2. Noise filtering

A further important step of preprocessing is smoothing which facilitates the succeeding segmentation as well as a preservation and enhancement of edges. We implemented an edge preserving smoothing filter [41]. It works similar to the widely known Kuhawara filter [46] by using a set of differently shaped filter masks. On each pixel position for all the masks the average gray value and the variance is calculated. Finally, the pixel value is chosen as the average gray value of the mask that overlaps the image region of the least variance. Compared to the Kuhawara filter, the extensions of the implemented algorithm are the usage of 21 filter masks and the repetition of filtering until changes are under a certain threshold.

In a last preprocessing step, noise was reduced by an *Adaptive Nonlinear Diffusion Smoothing* (ANDS) [4]. This ANDS method has an edge preserving behavior as well as a powerful smoothing characteristic. The iterative procedure of [4] was implemented. The iteration has been performed with a $(2S + 1 \times 2S + 1)$ filter-mask with scaling factor S according to

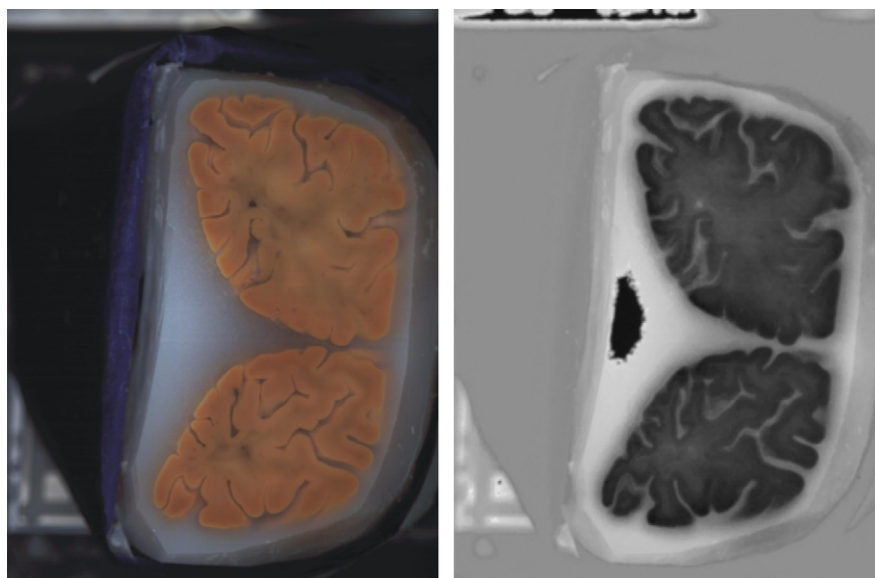


Fig. 2. The original image (left) and the color space transformed image.

$$I^{(t+1)}(\vec{x}) = \frac{\sum_{i=-S}^{+S} \sum_{j=-S}^{+S} I^{(t)}(x_1 + i, x_2 + j) \cdot w^{(t)}}{\sum_{i=-S}^{+S} \sum_{j=-S}^{+S} w^{(t)}} \quad (3)$$

where \vec{I} is a vector with one element, i.e., the gray value image, resp., a vector with three elements in the case of color images and $w^{(t)}$ the convolution kernel

$$w^{(t)}(x_1, x_2) = \exp\left(-\frac{|d^{(t)}(x_1, x_2)|^2}{2 \cdot k^2}\right) \quad (4)$$

with k as the variance of the filter-mask and $d^{(t)}(x_1, x_2)$ as the gradient in a 3×3 -window

$$d^{(t)}(x_1, x_2) = \sqrt{G_{x_1}^2 + G_{x_2}^2} \quad (5)$$

with

$$(G_{x_1}^2, G_{x_2}^2) = \left(\frac{\partial I^{(t)}(x_1, x_2)}{\partial x_1}, \frac{\partial I^{(t)}(x_1, x_2)}{\partial x_2}\right). \quad (6)$$

2.4. Segmentation

2.4.1. Adaptive fuzzy c-means segmentation

The preprocessed gray level images contain artifacts and intensity inhomogeneities which make it impossible to apply the standard fuzzy segmentation algorithm [12,7]. Continuous changes of intensity inhomogeneities can be counteracted by a so-called *gain field*, resp., *multiplier field* which has the same size like the underlying image. It is determined iteratively within each segmentation step for each pixel and its fuzzy membership to a certain class. The centers of classes are multiplied by the gain field $g_{(x,y)}$. The gain field is smooth and shows only small variations in the x - and y -direction. The two dimensional AFCM-algorithm minimizes the following objective function with regard to membership functions u , centroids \mathbf{v} and the gain field g :

$$J_{\text{AFCM}} = \sum_{x,y} \sum_{k=1}^K u_{(x,y),k}^q \| \mathbf{y}_{(x,y)} - g_{(x,y)} \cdot \mathbf{v}_k \|^2 + \lambda_1 \sum_{x,y} ((d_x * g_{(x,y)})^2 + (d_y * g_{(x,y)})^2) + \lambda_2 \sum_{x,y} ((d_{xx} * g_{(x,y)})^2 + 2(d_{xy} ** g_{(x,y)})^2 + (d_{yy} * g_{(x,y)})^2) \quad (7)$$

The parameters of J_{AFCM} are defined below:

q	weighting exponent on each fuzzy membership, resp., amount of fuzziness of the resulting classification)
$u_{(x,y)}$	membership function (see (8))
$g_{(x,y)}$	unknown <i>Gain Field</i>
\mathbf{v}	class center(s) or centroid(s) of class(es) k (see (9))
d_x, d_y	known finite operator of deviation along the columns and rows

λ_1, λ_2	term of first and second order regulation
*	one dimensional discrete convolution
**	two dimensional discrete convolution
d_{xx}	$d_{xx} = d_x * d_x$
d_{xy}	$d_{xy} = d_x ** d_y$

The parameters λ_1 and λ_2 should be adjusted with respect to the regularity of the inhomogeneities of intensities. For small fluctuations of intensities, resp., homogeneous distributions of intensities large λ_1 and λ_2 values should be chosen.

The function J_{AFCM} can be minimized by calculating the first derivative of J_{AFCM} with respect to $u_{(x,y),k}$, \mathbf{v}_k and $g_{(x,y)}$ and setting it to zero [12,7,29]. The algorithm for minimizing J_{AFCM} is listed below:

(1) Initialization

- (a) \mathbf{v}_k initialize for $k = 1, \dots, K$
- (b) $\forall x, y: g_{(x,y)} = 1$

(2) $\forall x, y$ and $k = 1, \dots, K$ calculate new membership values

$$u_{(x,y),k} = \frac{\| \mathbf{y}_{(x,y)} - g_{(x,y)} \mathbf{v}_k \|^2 / (q-1)}{\sum_{n=1}^K \| \mathbf{y}_{(x,y)} - g_{(x,y)} \mathbf{v}_n \|^2 / (q-1)} \quad (8)$$

(3) Calculate new centers of classes, for $k = 1, \dots, K$

$$\mathbf{v}_k = \frac{\sum_{x,y} u_{(x,y),k}^q \cdot g_{(x,y)} \cdot \mathbf{y}_{(x,y)}}{\sum_{x,y} u_{(x,y),k}^q \cdot g_{(x,y)}^2} \quad (9)$$

(4) Determine the new *Gain Field*

$$\sum_{k=1}^K u_{(x,y),k}^q \langle \mathbf{y}_{(x,y)}, \mathbf{v}_k \rangle = g_{(x,y)} \sum_{k=1}^K u_{(x,y),k}^q \langle \mathbf{v}_k, \mathbf{v}_k \rangle + \lambda_1 (H_1 * g)_{(x,y)} + \lambda_2 (H_2 * g)_{(x,y)} \quad (10)$$

The convolution kernels H_1 and H_2 are given by:

$$H_1(x, y) = d_x * \check{d}_x + d_y * \check{d}_y = \begin{pmatrix} 0 & -1 & 0 \\ -1 & 4 & -1 \\ 0 & -1 & 0 \end{pmatrix}$$

$$H_2(x, y) = d_{xx} * \check{d}_{xx} + 2(d_{xy} ** \check{d}_{xy}) + d_{yy} * \check{d}_{yy} = \begin{pmatrix} 0 & 0 & 1 & 0 & 0 \\ 0 & 2 & -8 & 2 & 0 \\ 1 & -8 & 20 & -8 & 1 \\ 0 & 2 & -8 & 2 & 0 \\ 0 & 0 & 1 & 0 & 0 \end{pmatrix}$$

Where \check{f} is the mirror reflection of the finite difference operator f with the notation $\check{f}(i) = f(-i)$ [31].

- (5) If the criterion of convergence is fulfilled the algorithm stops otherwise it proceeds with the next iteration at step 2.

The criterium of convergence is the maximal change of the membership for all pixels at two successive iterations. If the change is smaller than a threshold then the classification of the pixels for a single image terminates. We observed for the data set under investigation that a threshold of 0.01 provides optimal classification results.

We applied the algorithm for the initialization of class centers according to [29]. Because the AFCM algorithm is robust against false initializations of class centers we distributed the centers equidistantly over images and observed a fast adaption of the classification process to the classes.

The calculation of the *Gain Field* (10) is an expensive computation, therefore, the Jacobi-method was realized by a multi-grid algorithm [42].

The matrix form of the *Gain Field* (10) is

$$\mathbf{f} = \mathbf{W}\mathbf{m} + (\lambda_1\mathbf{H}_1 + \lambda_2\mathbf{H}_2) \mathbf{m} = \mathbf{A}\mathbf{m} \quad (11)$$

whereby $\mathbf{f} = \sum_{k=1}^K u_{(x,y),k}^q \langle \mathbf{y}_{(x,y)}, \mathbf{v}_k \rangle$ and $\mathbf{m} = g_{(x,y)}$ are brought into a vector. \mathbf{W} is a diagonal matrix with the elements $\sum_{k=1}^K u_{(x,y),k}^q \langle \mathbf{v}_k, \mathbf{v}_k \rangle$ on the diagonal, \mathbf{H}_1 and \mathbf{H}_2 are the versions of H_1 and H_2 and $\mathbf{A} = (\mathbf{W} + \lambda_1\mathbf{H}_1 + \lambda_2\mathbf{H}_2)$. The equation $\mathbf{f} = \mathbf{A}\mathbf{m}$ is solved to \mathbf{m} by determining the inverse \mathbf{A}^{-1} for \mathbf{A} .

If $\mathbf{A} = \mathbf{D} - \mathbf{L} - \mathbf{U}$ has been decomposed with \mathbf{D} the diagonals, \mathbf{L} the lower negative triangular matrix and \mathbf{U} the upper negative triangular matrix of \mathbf{A} then we obtain the weighted Jacobi-Iteration by the following rule:

$$\mathbf{m}^{(i+1)} = [(\mathbf{1} - \omega)\mathbf{I} + \omega\mathbf{D}^{-1} (\mathbf{L} + \mathbf{U})]\mathbf{m}^i + \omega \mathbf{D}^{-1}\mathbf{f} \quad (12)$$

with \mathbf{I} as the identity matrix and ω as a parameter of weighting ($\omega = 0.3$ has been proved and used for all images).

If \mathbf{v} is an approximation of the solution of \mathbf{m} then the error is determined by $\mathbf{e} = \mathbf{m} - \mathbf{v}$. The error \mathbf{e} satisfies the differential equation $\mathbf{A}\mathbf{e} = \mathbf{r}$ whereby $\mathbf{r} = \mathbf{f} - \mathbf{A}\mathbf{v}$ is residual. The *REDUCE*-Operator transforms the *Gain Field* at a large resolution to its half and the *EXPAND*-Operator expands each pixels at a coarse resolution according to its (2×2) -neighborhood up to its original resolution.

2.4.2. Fuzzy and noise tolerant adaptive segmentation

To improve the behavior of the AFCM fuzzy classification with respect to noise the *Fuzzy and Noise Tolerant Adaptive Segmentation Method* (FANTASM) has been implemented [28].

$$J_{\text{FANTASM}} = J_{\text{AFCM}} + \frac{\beta}{2} \sum_{x,y} \sum_{k=1}^K u_{(x,y),k}^q \sum_{n \in N_{(x,y)}} \sum_{m \neq k} u_{n,m}^q \quad (13)$$

The following new parameters are used:

- β determines the smoothness of the membership function and is determined empirically.
- $N_{(x,y)}$ the set of neighborhood pixels.

The steps of the FANTASM-algorithm are listed below:

- (1) Initialization
 - (a) \mathbf{v}_k initialize for $k = 1, \dots, K$
- (2) $\forall x, y$ and $k = 1, \dots, K$ the membership values

$$u_{(x,y),k} = \frac{(\|\mathbf{y}_{(x,y)} - g_{(x,y)}\mathbf{v}_k\|^2 + \beta \sum_{n \in N_{(x,y)}} \sum_{m \neq k} u_{n,m}^q)^{-1/(q-1)}}{\sum_{i=1}^K (\|\mathbf{y}_{(x,y)} - g_{(x,y)}\mathbf{v}_i\|^2 + \beta \sum_{n \in N_{(x,y)}} \sum_{m \neq i} u_{n,m}^q)^{-1/(q-1)}} \quad (14)$$

- (3) New calculation of the *Gain Field*

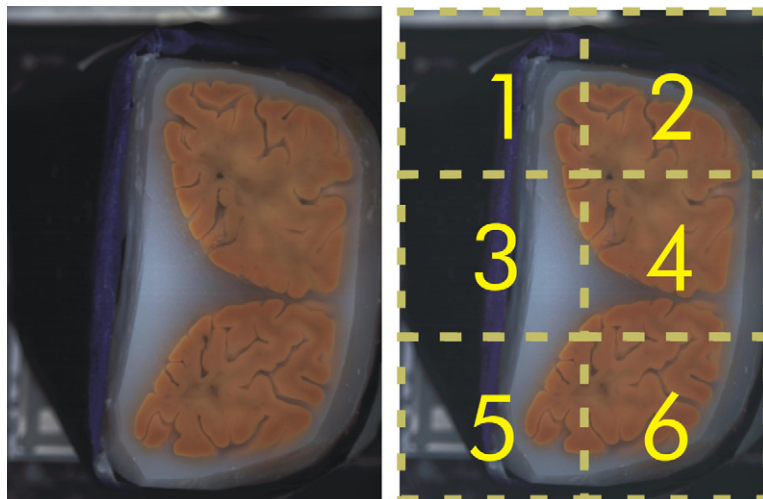


Fig. 3. (Left): Image before segmentation. (Right): Lattice containing 6 image sectors.

$$\sum_{k=1}^K u_{(x,y),k}^q \langle \mathbf{y}_{(x,y)}, \mathbf{v}_k \rangle = g_{(x,y)} \sum_{k=1}^K u_{(x,y),k}^q \langle \mathbf{v}_k, \mathbf{v}_k \rangle + \lambda_1 (H_1 * g)_{(x,y)} + \lambda_2 (H_2 * g)_{(x,y)} \quad (15)$$

(4) Calculate the new centers of classes for $k = 1, \dots, K$

$$\mathbf{v}_k = \frac{\sum_{x,y} u_{(x,y),k}^q \cdot \mathbf{y}_{(x,y)}}{\sum_{x,y} u_{(x,y),k}^q} \quad (16)$$

(5) If the criterium of convergence is fulfilled the procedure stops otherwise it proceeds with the succeeding iteration at step 2.

2.4.3. Parallelization of AFCM and FANTASM

Due to large image sizes, image contents and parameters of AFCM and FANTASM the computation on a sequential von-Neumann-architecture is relatively expensive. For one image of the data set under investigation an Intel PIII 1 GHz machine running under Linux needs 5:10:28 h. Therefore, it is mandatory to develop efficient algorithms for efficient hardware.

Thus, we implemented the segmentation on a parallel computer, a 72 processor shared memory 64 bit architecture (SUN sf15k). For parallel computation, each image is partitioned into disjoint sectors, where sectors are processed by threads. These threads – similar to processes – run in parallel, either by time division or on several processors under control of the operating system. For the demands of the classification algorithms used here it is necessary to perform a synchronization of threads, especially for the calculation of convolutions which makes point operations necessary. (Fig. 3)

To determine the number of threads in x - and y -direction the following scheme was used (n : size of image in x -direction, m : size of image in y -direction):

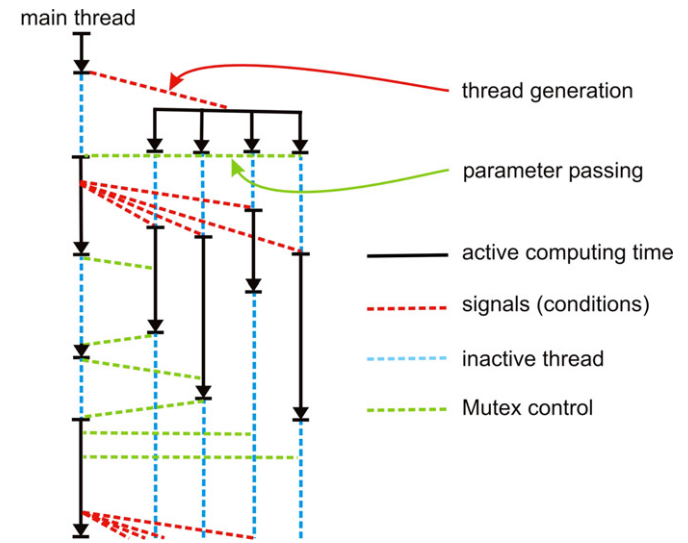


Fig. 4. The synchronization of threads and their relative use of computing time is shown here.

$$f_{\text{norm}} = \sqrt{\frac{n \cdot m}{\text{\#desired Threads}}} \quad (17)$$

$$\text{\#Threads in } x\text{-direction} = \text{round}\left(\frac{n}{f_{\text{norm}}}\right)$$

$$\text{\#Threads in } y\text{-direction} = \text{round}\left(\frac{m}{f_{\text{norm}}}\right)$$

Naturally, a maximal partition into single pixels does not make sense, therefore, the number of threads is restricted by:

$$n, m \geq f_{\text{norm}} \geq 32.$$

In practice, all threads for one image were generated at the beginning of a calculation, thereafter the corresponding threads for certain calculations were activated by the main

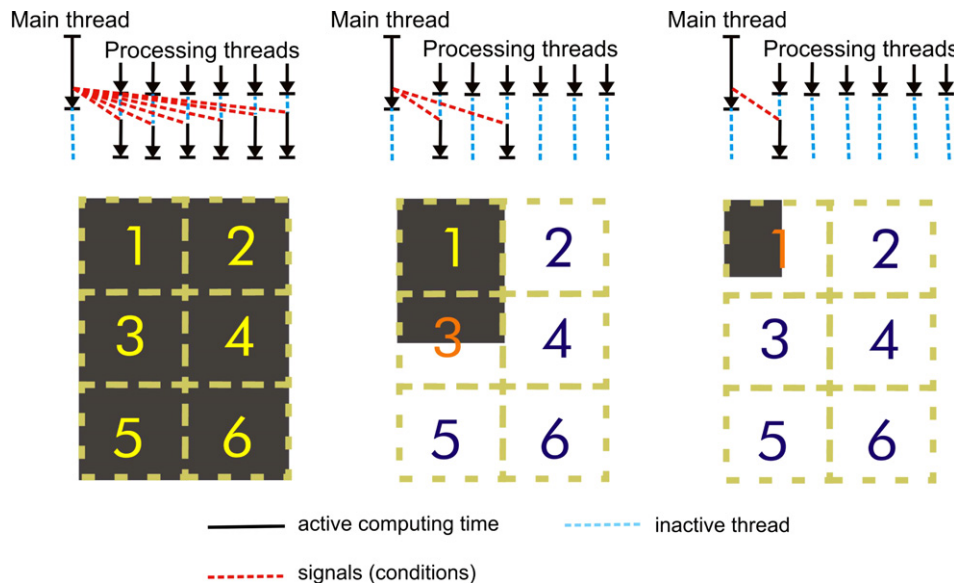


Fig. 5. The access of the parallel multi-grid algorithm to sectors and regions within sectors of an image at different resolutions.

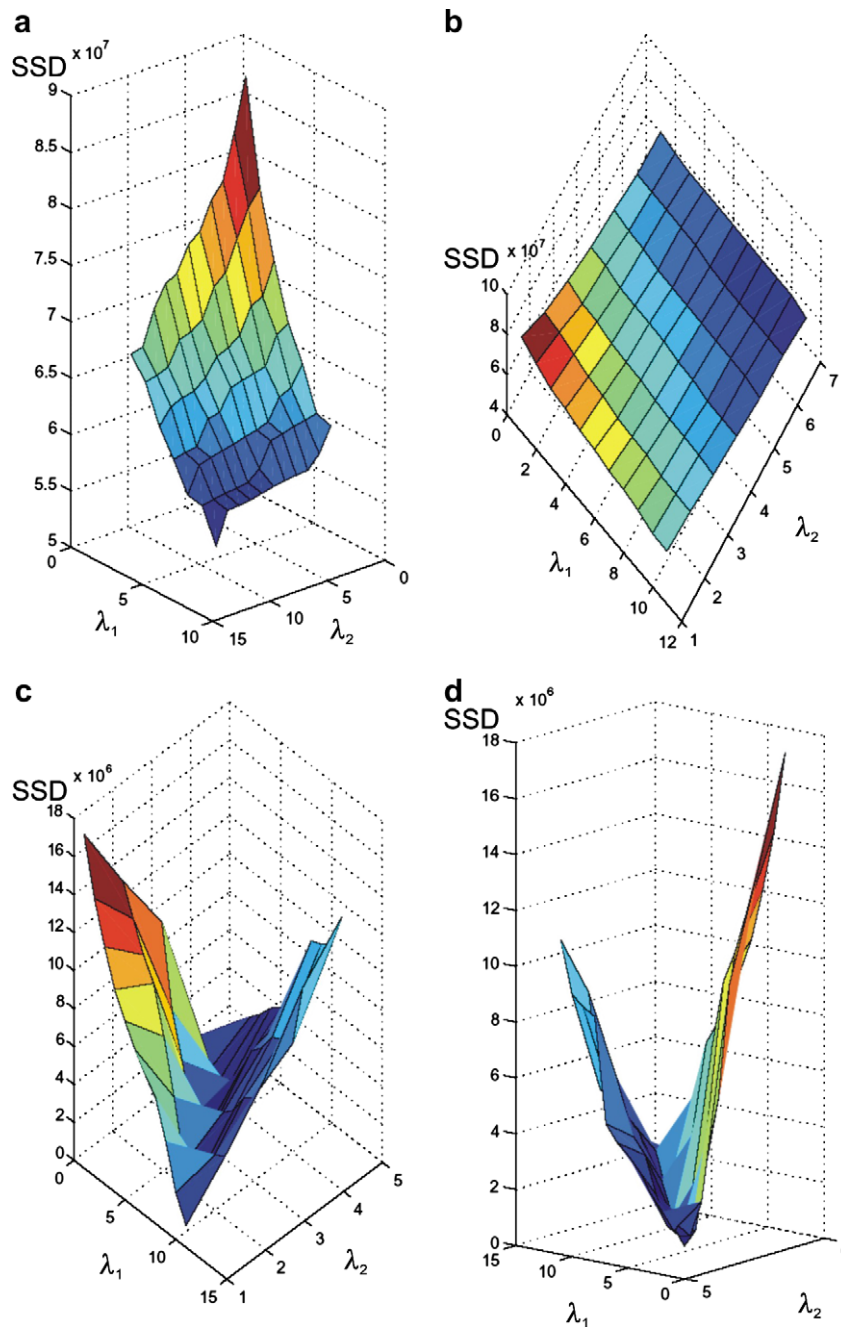


Fig. 6. The SSDs within different parameter spaces for two adjacent images are shown. In (a) and (b) the local minimum of SSD lies at the border of the parameter space. In (c) and (d) an optimal local minimum was determined.

thread if certain conditions are fulfilled. The threads were synchronized as shown in Fig. 4.

The calculation of the *Gain Fields* consists of a convolution operation (formula 12) that can be parallelized by allocation of additional memory. The multi-grid approach for solving the differential equation was parallelized by assigning the pixel sets at different resolutions of each sector to a certain thread. If the resolutions are coarser the parallelism decreases until only one thread per sector is active. Using this scheme a meaningful partition of an image to threads can be maintained and the synchronization is kept minimal (Fig. 5).

At least, the main thread calculates in a sequential part the result, resp., the new centers of classes and saves the results as a segmented image.

2.4.4. Optimal parameters

As already pointed out λ_1 and λ_2 have to be initialized for AFCM and β , n (n : neighborhood) for FANTASM. A suitable value for λ_1 is 2×10^5 and for λ_2 is 2.75×10^5 ($\lambda_1 < \lambda_2$) for a pre-segmentation with 5 classes and for a final segmentation with 3 classes λ_1 is 2×2.5^4 and for λ_2 are 4×10^4 leads to reasonable results. Finally, a bilevel image masks the intensity values of the non-segmented

image. In order to control the segmentation and to observe effects at critical regions 3 classes were calculated. However, we observed strong over- and under-segmentations specially at those images exhibiting larger deviations from the mean intensity and variance of the image statistics. Because the parameter space is relative large and small changes of parameters leads to large differences of the segmentations results we implemented an approximation to the optimal parameter set for a particular segmentation. A measure for the difference of two adjacent images b_i, b_j is the *Sum Squared Difference Mass (SSD)* (Fig. 6).

$$SSD(b_i, b_j) = \sum_{x=0}^{m-1} \sum_{y=0}^{n-1} (b_{i(x,y)} - b_{j(x,y)})^2. \quad (18)$$

If a *SSD* is larger than a threshold which is dependent on image size, variance and mean intensity the segmentation of all images exhibiting the optimal segmentation is determined interactively and thereafter an optimization procedure of certain parameters within a predefined search space can variate the parameters (multi parameter optimization) until the minimal *SSD* is reached. The step size for searching the $\lambda_1, \lambda_2, \beta$ parameter space can be predefined. The optimization can be performed either over a certain search space (multi parameter mode) or until *SSD* does not decrease any more (automatic mode). In Fig. 6 local minima within a search space of λ_1 and λ_2 are shown.

We have tested the automatic mode for those images that show strong changes of their pixel statistic and

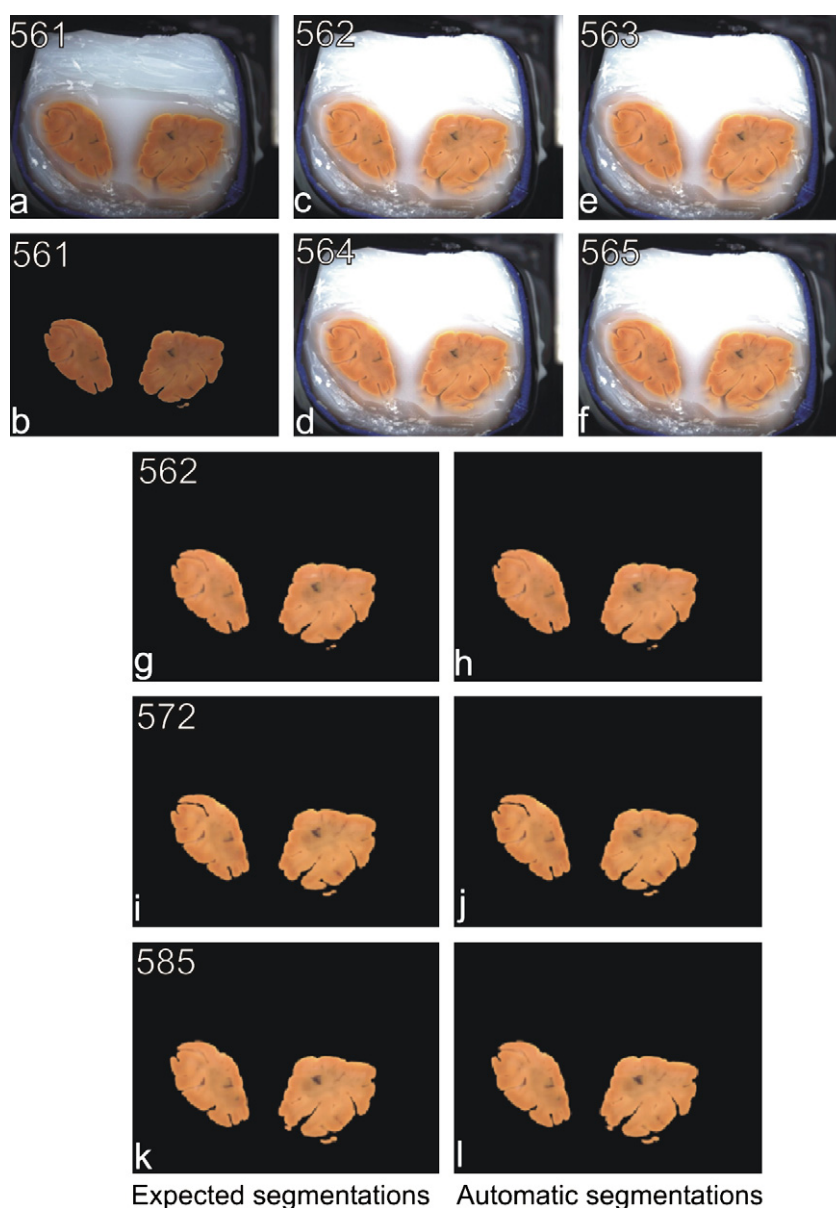


Fig. 7. (a) Shows the original image before segmentation. (b) The segmented foreground of the original image (a). (c)–(f) Show four consecutive images which have a much larger brightness than the preceding image 561 in (a). (h), (j), (l) The parameters for the segmentations of images 562, 572, and 585 are determined automatically and are not disturbed by images (c)–(f). (g), (h) and (i) display the expected segmentations which were obtained interactively. The automatic segmentation was as good as the interactive resp. optimal segmentation where parameters were optimized by an investigator.

obtained a satisfying segmentation which is obviously better than without parameter optimization (Fig. 7).

3. Results

To compare the segmentation results of the AFCM and FANTASM method (Fig. 8) alternative segmentations of image 3005 were generated. The Otsu-method [24], a local median threshold technique [9], the region growing approach [16], the minimum of the smoothed gray level frequencies [34,40] and local adaptive segmentation [36].

3.1. Segmentation results

The segmentation method of Otsu leads to the best results among the alternative approaches. Oversegmentation and coinstantaneous segmentation of details like small sulci produces results comparable with AFCM and FANTASM. The local median threshold technique [9] and the minimum of the smoothed gray level frequencies are relative similar whereby the latter provides better segmentations at the cortical surface. The local median threshold segmentation show the tendency to slight undersegmentation. The adaptive thresholding methods segments small objects located within the background and classifies pixels of the paraffin wax phase at the cortex border to the foreground. Therefore, these methods provide a slight oversegmentation. The region growing approach delivers a oversegmentation especially within the foreground leading to holes within the striatum (Figs. 8, 9).

The same ROI of each segmentation consolidate the impression of the comparisons of whole image segmenta-

tions. In Fig. 10 the large oversegmentations by the adaptive and the region growing method are noticeable. The Otsu and the histogram minima method show best results among the conventional segmentation algorithms with respect to over- and undersegmentations. The AFCM method provides less oversegmentation than the FANTASM method whereby the latter shows better segmentation results of small sulci.

3.2. 3D-reconstruction

After segmentation of all block-face images we performed a homogenization of the image statistic and generated a three dimensional reconstruction (Fig. 11). The coarse sulci and gyri pattern can be detected easily and are used now to relate sulci and gyri of the appropriate coronal histologic sections.

As already mentioned, the duration of the ACFM method on a single processor using one thread takes 5:10:28 h.

3.3. Results of parallelization

Using 64 processors, the segmentation of a single image could be speed up by factor 23. The efficiency of parallelization, defined as speed up per used number of processors is 0.36. In order to use the full performance of the machine, the program allows to segment multiple images in parallel. In a configuration of 15 threads per image and 16 image segmentations in parallel we could reach an efficiency of 0.95. For each image about five minutes were needed. Compared to the time on a single processor, a speed up of about 60 using

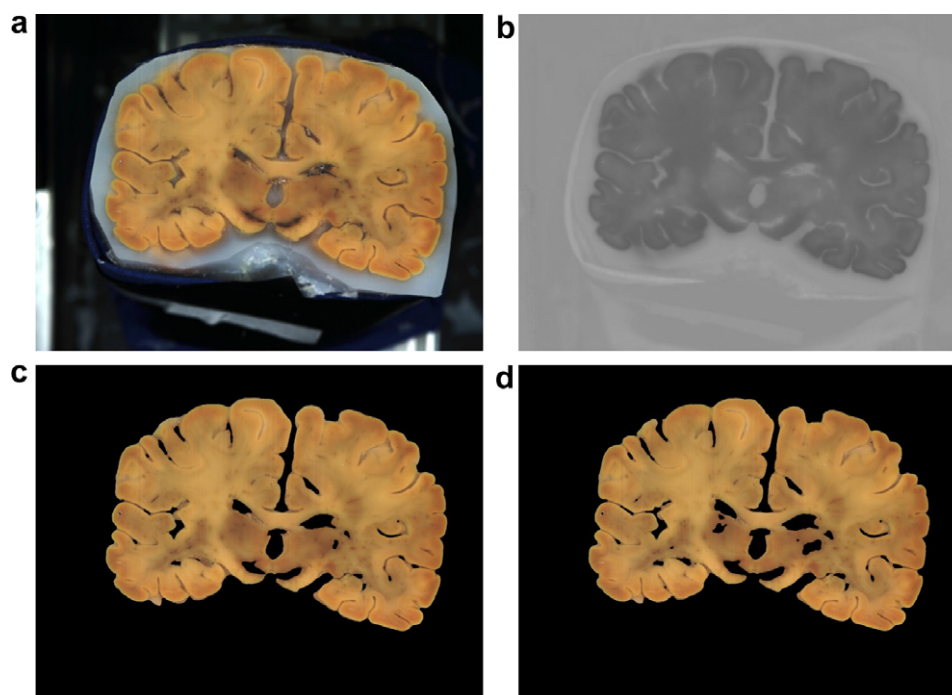


Fig. 8. Segmentation results of image 3005: (a) original image, (b) preprocessed image, (c) AFCM, (d) FANTASM.

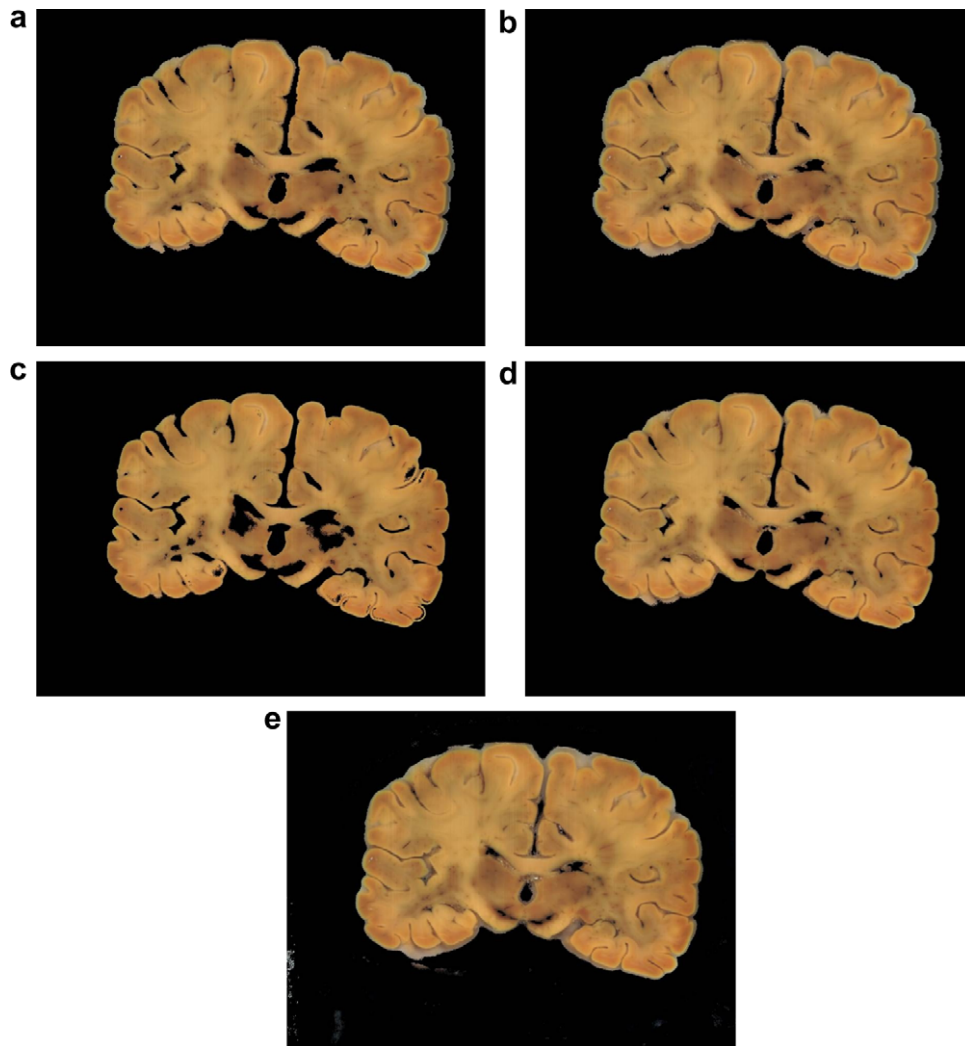


Fig. 9. Image 3005 segmented by: (a) Otsu, (b) mean intensity, (c) region growing, (d) histogram-minima, (e) adaptive. White arrows: undersegmentations, red arrows: oversegmentations.

64 processors is reached. Generally, a mixture of intra image parallelization and processing of multiple independent images is a proper way to exploit the computing power of shared memory multiprocessor systems.

4. Discussion

A whole human brain was sectioned serially and sections were mounted on glass slides for succeeding processing and analysis. The sections are deformed and do not match spatially anymore. To perform an exact registration it is necessary to align them with undistorted reference images before sectioning. Therefore, a block-face image before each sectioning was produced. The block-face image contain artifacts mainly caused by illumination changes and slight focusing errors. Therefore, a segmentation technique must be realized that manage these disturbances to produce accurate and robust segmentations of the foreground class in each image. However, suitable algorithms which make use of statistical procedures are computational expensive. Thus, a parallel version of the AFCM and FANTASM

algorithms for a memory shared architecture have been developed. Color images have been preprocessed to obtain appropriate data for accurate and robust segmentation. AFCM and FANTASM produced optimal segmentation results after performing a parameter optimization. Using this extension the whole series of 6213 images can be segmented.

The advantage of the memory shared architecture consists in the common access of all threads to the whole range of memory addresses. A further advantage for FANTASM is that different ranges of memory used in parallel by different threads of the algorithm must not be interchanged after each iteration. Furthermore, thread-programming is portable to other architectures (single processor and multiprocessor platforms).

The AFCM produces slightly undersegmentations especially at the boarder of the cortical surface and within deep and small sulci. In contrast, FANTASM detects boards of small sulci to a certain degree, however, slight oversegmentations occur within those subcortical regions sharing similar intensity statistics like image regions within small sulci.

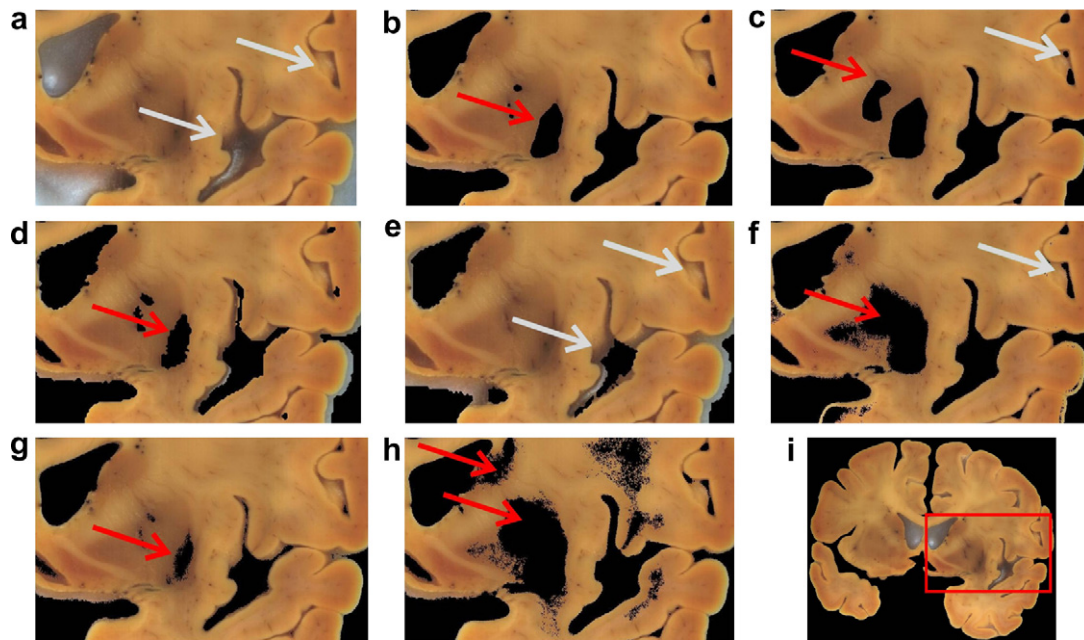


Fig. 10. ROI of image 3960: (a) original image, (b) AFCM, (c) FANTASM, (d) Otsu, (e) mean intensity, (f) region growing, (g) histogram-minimum, (h) adaptive, (i) marked ROI.

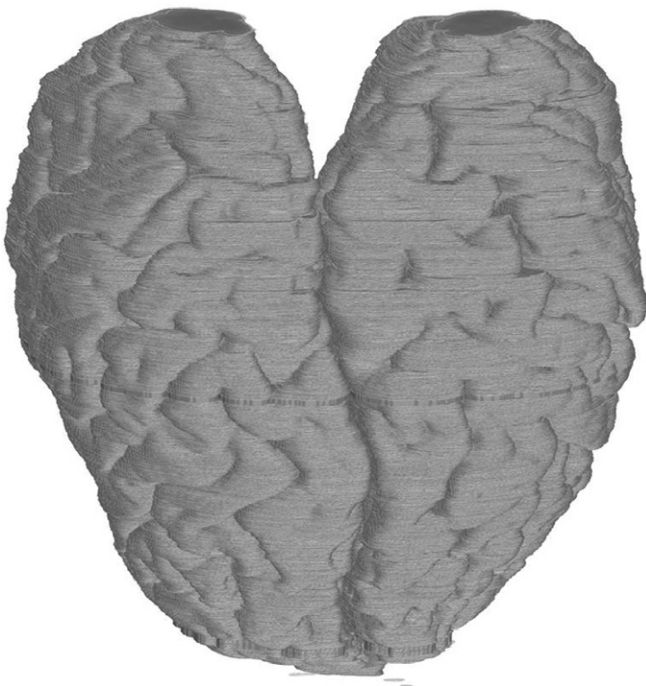


Fig. 11. Reconstruction of all segmented block-face images.

In comparison with conventional segmentation algorithms the same problems of over- and undersegmentations are observed. Due to the size of 46 GB we performed a comparison for a small sample of images for the conventional methods only. Hence, these methods were not tested in an semi automatic mode over the whole image stack like the AFCM and FANTASM methods. However, dramatic over- and undersegmentations especially within critical

foreground regions like the subcortical area and the cortical surface can be expected.

Definitely, there exist other sophisticated methods, e.g., Markov random field based segmentation [6,44,18,14], multilevel, resp., scale-space approaches [20], anisotropic filtering [3] segmentation based on genetic algorithms [47,13,22], neural networks [48,1], hybrid segmentation techniques [32], statistical procedures [19,49,2] and adaptive weight smoothing [33]. A qualitative and quantitative comparison of conventional segmentation operators was tested for small samples (Fig. 8–10). They were not applied to the stack of images because we concentrated on solving the problem of segmenting a complex image scene within a extraordinary large data set at reasonable time. Based on this spadework data can be compared easily with results obtained from other sophisticated segmentation operators.

The developed parallelization enables us now segmenting large datasets of serially sectioned paraffin mouse and rat brains as well for morphologic phenotyping and high through put analysis. These histologic sections may be up to 4 times thinner and end up with approximately 4000 coronal sections. Therefore, an efficient parallelization and robust algorithm is a necessary condition to perform comprehensive segmentation tasks on histologic data sets.

An interesting prospect would be a succeeding fine segmentation of a dilated and filled version of the presegmented data set with the three dimensional version [30] of the FANTASM method to obtain accurate segmentations of fine sulci and a concurrent preservation of subcortical structures belonging to the foreground.

First of all, an important step for coregistration with high resolution histologic data down to single cell data of

the Human Neuroscanning Project have been completed and we are now able to reconstruct spatially exact locations of cell populations in this histologic data set of a human brain.

Acknowledgements

We thank U. Almert, P. Lau, E. Mecke of the Institute of Anatomy (University of Lübeck) for their excellent histologic preparations, digitizing and data administration, W. Kühnel (Institute of Anatomy, Medical University Lübeck) for his extensive support. We are grateful for support and critical discussion of this study by A. Wree (University of Rostock, Institute of Anatomy). This work was supported by funds of the Peter Dornier, Gerhard Ten Door-kaat Koolman and the Possehl foundation.

References

- [1] J. Alirezaie, M. Jernigan, C. Nahmias, Neural network-based segmentation of magnetic resonance images of the brain, *IEEE Trans. Nuc. Sci.* 44 (1997) 194–198.
- [2] U. Amato, M. Larobina, A. Antoniadis, B. Alfano, Segmentation of magnetic resonance brain images through discriminant analysis, *J. Neurosci. Meth.* 131 (2003) 65–74.
- [3] M. Atkins, B. Mackiewicz, Fully automatic segmentation of the brain in MRI, *IEEE Trans. Med. Imag.* 17 (1998) 98–107.
- [4] D. Barash, D. Comaniciu, A common framework for nonlinear diffusion, adaptive smoothing, bilateral filtering and mean shift, *IVC* 22 (2004) 73–81.
- [5] E. Bardinnet, S. Ourselin, D. Dormont, G. Malandain, D. Tandé, K. Parain, N. Ayache, J. Yelnik, Co-registration of histological, optical and MR data of the human brain, *LNCS* 2488 (2002) 548–555.
- [6] Barker, S.A., Rayner, P.J.W., 1997. Unsupervised image segmentation using markov random field models. In: *Energy Minimization Methods in Computer Vision and Pattern Recognition*, pp. 165–178. URL: citeseer.ist.psu.edu/barker97unsupervised.html.
- [7] J. Bezdek, A convergence theorem for the fuzzy ISODATA clustering algorithms, *IEEE Trans. PAMI* 2 (1980) 1–8.
- [8] J. Bezdek, L. Hall, L. Clarke, Review of mr image segmentation techniques using pattern recognition, *Med. Phys.* 20 (1993) 1033–1048.
- [9] Bock, S., 2002. Segmentierung, Deagglomeration und Morphometrie von Zellen in Großschnitten des menschlichen Vorderhirns. Tech. rep., University of Lubeck, Institute of Anatomy, Institute of Mathematics, Studien-arbeit.
- [10] L. Brown, A survey of image registration techniques, *ACM Computing Surveys* 24 (1992) 325–376.
- [11] A. Colchester, A. Roche, Y. Zhu, Y. He, S. Ourselin, B. Nailon, S. Hojjat, J. Ironside, S. Al-Sarraj, N. Ayache, J. Wardlaw, Registration of reconstructed post mortem optical data with MR scans of the same patient, *LNCS* 2208 (2001) 957–965.
- [12] J. Dunn, A fuzzy relative of the isodata process and its use in detecting compact well-separated cluster, *J. Cyb.* 3 (1973) 32–57.
- [13] Y. Fan, T. Jiang, Volumetric segmentation of brain images using parallel genetic algorithms, *IEEE Trans. Med. Imag.* 21 (2002) 904–909.
- [14] F. Forbes, N. Peyrard, Hidden Markov random field model selection criteria based on mean field-like approximations, *IEEE Trans. PAMI* 25 (2003) 1089–1101.
- [15] C. Glasbey, An analysis of histogram-based thresholding, *CVGIP* 55 (1993) 532–537.
- [16] R. Gonzales, R. Woods, *Digital image processing*, Addison-Wesley Publishing Company, Reading, 1993.
- [17] R. Haralick, L. Shapiro, Image segmentation techniques, *CVGIP* 29 (1985) 100–132.
- [18] D. Hochbaum, An efficient algorithm for image segmentation, markov random fields and related problems, *J. ACM* 48 (4) (2001) 686–701.
- [19] T. Kapur, W. Eric, L. Crimson, W. Wells, R. Kikinis, Segmentation of brain tissue from magnetic resonance images, *Med. Image Anal.* 1 (1996) 109127.
- [20] T. Lindeberg, P. Lidberg, P. Roland, Analysis of brain activation patterns using a 3-D scale-space primal sketch, *Hum. Brain Map.* 7 (1999) 166–194.
- [21] A. MacKenzie-Graham, E. Lee, I. Dinov, M. Bota, D. Shattuck, S. Ruffins, H. Yuan, F. Konstantinidis, A. Pitiot, Y. Ding, G. Hu, R. Jacobs, A. Toga, A multimodal, multidimensional atlas of the C57BL/6J mouse brain, *J. Anat.* 204 (2004) 93–102.
- [22] K. Matsui, Y. Suganami, Y. Kosugi, Feature selection by genetic algorithm for MRI segmentation, *Sys. Comp. Japan* 30 (1999) 69–78.
- [23] J. Modersitzki, *Numerical Methods for Image Registration*, Oxford University Press, New York, 2004.
- [24] N. Otsu, A threshold selection method from gray level histograms, *IEEE Trans. Sys. Man. Cyb.* 9 (1979) 62–66.
- [25] S. Ourselin, E. Bardinnet, D. Dormont, G. Malandain, A. Roche, N. Ayache, D. Tandé, K. Parain, J. Yelnik, Fusion of histological sections and MR images towards the construction of an atlas of the human basal ganglia, *LNCS* 2208 (2001) 743–751.
- [26] S. Ourselin, A. Roche, G. Subsol, X. Pennec, N. Ayache, Reconstructing a 3d structure from serial histological sections, *IVC* 20 (2000) 25–31.
- [27] N. Pal, S. Pal, A review on image segmentation techniques, *Pat. Rec.* 26 (1993) 1277–1294.
- [28] D. Pham, Robust fuzzy segmentation of magnetic resonance images, *Proc. 14th IEEE Symp. Comp-Based Med. Syst. (CBMS2001)* (2001) 127–131.
- [29] D. Pham, J. Prince, An adaptive fuzzy c-means algorithm for image segmentation in the presence of intensity inhomogeneities, *Pat. Rec. Lett.* 20 (1999) 57–68.
- [30] D. Pham, J. Prince, An adaptive fuzzy segmentation algorithm for three-dimensional magnetic resonance images, *LNCS* 1613 (1999) 140–153.
- [31] D. Pham, J. Prince, Adaptive fuzzy segmentation of magnetic resonance images, *IEEE Trans. Med. Imag.* 18 (1999) 737–752.
- [32] A. Pitiot, A. Toga, P. Thompson, Adaptive elastic segmentation of brain MRI via shape-model-guided evolutionary programming, *IEEE Trans. Med. Imag.* 21 (2002) 910–923.
- [33] J. Polzehl, V. Spokoyny, Adaptive weights smoothing with applications to image segmentation, *J. Royal Stat. Soc.* 62 (2000) 335–354.
- [34] J. Prewitt, M. Mendelsohn, The analysis of cell images, *Ann. N.Y. Acad. Sci.* 128 (1966) 1035–1053.
- [35] S. Ranade, J. Prewitt, A comparison of some segmentation algorithms for cytology, *ICPR80* (1980) 561–564.
- [36] A. Rosenfeld, *Digital picture processing*, Vol. 2, Academic Press, New York, 1982.
- [37] P. Sahoo, S. Soltani, A. Wong, Y. Chen, A survey of thresholding techniques, *CVGIP* 41 (1988) 233–260.
- [38] S. Sangwine, R. Horne, *The colour image processing handbook (Optoelectronics Imaging and Sensing)*, Kluwer Academic Publishers., 1998.
- [39] Schmitt, O., 2001. Die multimodale Architektur des menschlichen Gehirns. Vol. 1.
- [40] M. Sieracki, S. Reichenbach, K. Webb, Evaluation of automated threshold selection methods for accuratelay sizing microscopic fluorescent cells by image analysis, *Appl. Env. Micro.* 55 (1989) 2762–2772.
- [41] Somboonkaew, A., Chitwong, S., Cheevasuvit, F., Dejhan, K., Mitatha, S., 1999. Segmentation on the edge preserving smoothing image. *Proc. of the 20th Asian Conference on Remote Sensing (ACRS99)* 20, 1.

- [42] Staudacher, J., 2002. Multigrid methods for matrices with structure and applications in image processing. Ph.D. thesis, Technische Universität München, Institut für Informatik, München.
- [43] M. Szegin, B. Sankur, Survey over image thresholding techniques and quantitative performance evaluation, *J. Elect. Imag.* 13 (2004) 146–165.
- [44] T. Szirányi, J. Zerubia, L. Czúni, D. Geldreich, Z. Kato, Image segmentation using Markov random field model in fully parallel cellular network architectures, *Real-Time Imaging* 6 (2000) 195–221.
- [45] A. Toga, Postmortem anatomy from cryosectioned whole human brain, *J. Neurosci. Meth.* 54 (1994) 239–252.
- [46] R. van den Boomgaard, Decomposition of the Kuwahara-Nagao operator in terms of a linear smoothing and a morphological sharpening, *Proc. Int. Symp. Math. Morphol. VI (ISMM2002)* (2002) 283–292.
- [47] Veenman, C., Reinders, M., Backer, E., 2003. A cellular coevolutionary algorithm for image segmentation. *IEEE Trans. Image Proc* 12, 304–316. URL citeseer.ist.psu.edu/veenman01cellular.html.
- [48] Y. Wang, T. Adal, S.-Y. Kung, Z. Szabo, Quantification and segmentation of brain tissues from MR images: A probabilistic neural network approach, *IEEE Trans. Imag. Proc.* 7 (1998) 1165–1181.
- [49] W. Wells, W. Grimson, R. Kikinis, F. Jolesz, Adaptive segmentation of mri data, *IEEE Trans. Med. Imag.* 15 (1996) 429–442.
- [50] J. Weszka, A survey of threshold selection techniques, *CGIP* 7 (1978) 259–265.
- [51] R. Wilson, C.-T. Li, A class of discrete multiresolution random fields and its application to image segmentation, *IEEE Trans. PAMI* 25 (2002) 42–56.
- [52] Y. Zhang, A survey on evaluation methods for image segmentation, *Pat. Rec.* 29 (1996) 1335–1346.
- [53] Y. Zhang, Evaluation and comparison of different segmentation algorithms, *Pat. Rec. Let.* 18 (1997) 963–974.